

Understanding the Mechanism for Ribonucleotide Reductase Inactivation by 2'-Deoxy-2'-methylenecytidine-5'-diphosphate

M. A. S. Perez, P. A. Fernandes, and M. J. Ramos*

REQUIMTE, Faculdade de Ciências, Universidade do Porto, Rua do Campo Alegre, 687, 4169-007 Porto, Portugal

Received April 24, 2010

Abstract: Ribonucleotide reductase (RNR) is the key enzyme in the biosynthesis of deoxyribonucleotides. The enzyme has thus an attractive target for chemotherapies that fight proliferation-based diseases. 2'-Deoxy-2'-methylenecytidine-5'-diphosphate (CH_2dCDP) is a potent mechanism-based inhibitor of the enzyme RNR, which decomposes to an active alkylating furanone specie. The details of the inhibition mechanism are unknown, and experimental studies have indicated that some properties of the inactivation are dissimilar to those observed with a number of 2'-substituted 2'-deoxynucleotides mechanism-based inhibitors. To disclose the mechanism involved in RNR inactivation by CH_2dCDP we explored the potential-energy surface in two different models of the system with different objectives in mind. In order to conveniently explore the reactional space, i.e. to study the possible reactions between the CH_2dCDP and the RNR, we used a small model representing the active site of RNR with CH_2dCDP using DFT. To provide further insights and efficiently account for the long-range RNR– CH_2dCDP interactions and the stereochemical strain imposed by the protein scaffold we performed theoretical calculations on the more promising reactions using hybrid QM/MM calculations on a larger model system. We used quantum mechanics for the active-site region (CH_2dCDP and active-site residues) and molecular mechanics for the surroundings (6373 atoms of the R1 monomer). The results obtained led us to understand the correct mechanism for RNR inactivation by CH_2dCDP , and the furanone species formed presumably explains the dissimilarities observed with a number of 2'-substituted 2'-deoxynucleotides.

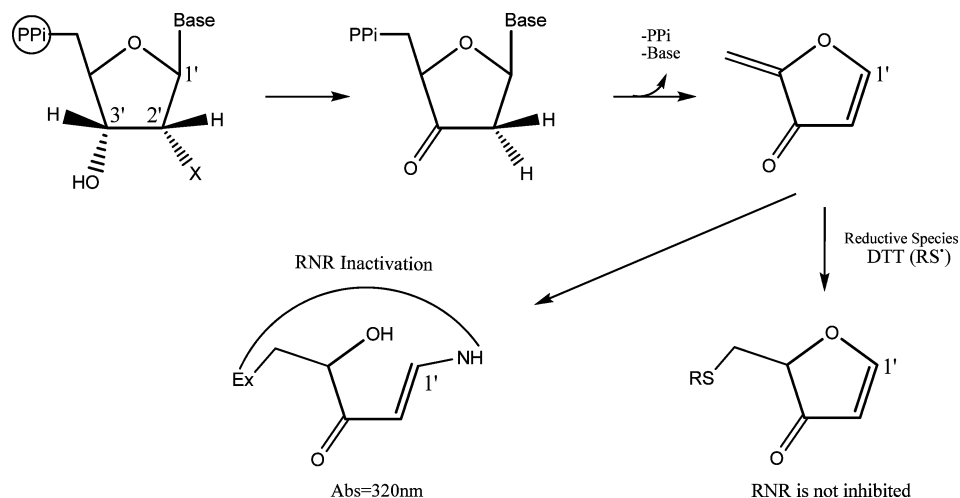
Introduction

The reduction of ribonucleotides into deoxyribonucleotides is strictly conserved in all living organisms and catalyzed by ribonucleotide reductase (RNR). This key role makes the RNR involvement a rate-limiting step in DNA replication and repair, turning it into an attractive target for antitumor, antiviral, and antibacterial therapies.^{1–8}

Different organisms have related RNRs, and their catalytic mechanism is always based on radical-mediated reactions.⁹ The *Escherichia coli* (*E. coli*) RNR is similar to the mammalian RNR and has served as its prototype in experimental and theoretical studies. *E. coli* RNR is consti-

tuted by two different homodimeric subunits. The larger one, known as R1 (761 residues), lodges the active site (for reduction of purines and pyrimidines) and three independent allosteric sites (specificity site, adenine specific site and hexamerization site).^{10,11} The smaller subunit, known as R2 (375 residues), contains a tyrosyl radical that is stabilized by an oxo-bridged binuclear Fe(III) complex.^{12,13} The active-site residues that are catalytically important are Cys225, Cys439, Cys462, Glu441, and Asn437. For catalysis to take place, the tyrosyl radical in R2 must generate a thyl one in Cys439 of the R1 active site. The catalysis can only occur when the tyrosyl radical migrates from subunit R2 to subunit R1 active site. The electron migration is thought to occur by proton-coupled electron transfers, through a ca. 35 Å long

* Corresponding author e-mail: mjramos@fc.up.pt.

Scheme 1. RNR Inactivation by 2'-Halo-2'-deoxynucleoside-5'-diphosphate²⁴

chain of hydrogen-bonded residues.^{14–20} The substrates of RNR are ribonucleosides-5'-diphosphates.

Different strategies for inactivation of RNR have been reported, namely, several modifications of the nucleotides' ribose moiety at the 2' and 3' positions have produced potent mechanism-based inhibitors. 2'-Deoxy-2'-methylencytidine-5'-diphosphates (*CH*₂dNDPs) are included among them.²¹ 2'-Deoxy-2'-methylidene-nucleosides (*CH*₂dN) were synthesized by Takenuki et al.²² in 1988 and have been demonstrated to possess antitumor activity.²³ It has been found that 2'-deoxy-2'-methylideneuridine-5'-diphosphates (*CH*₂dUDP) and 2'-deoxy-2'-methylidenecytidine-5'-diphosphates (*CH*₂dCDP) function as irreversible inactivators of RNR, but *CH*₂dCDP is a much more potent inhibitor. Experimental studies have shown that the inactivation is initiated by carbon C3'–H bond cleavage resulting in a 3'-keto-2'-methyldeoxyribonucleotide as the end product.²¹ The collapse of this into a furanone derivative occurs only in solution, later becoming attached to protein R1 and inhibiting the enzyme. The inhibition process is detected experimentally by a rapid increase in absorbance at 326 nm, and the rate of appearance of this band is similar to the rate of inactivation. However, this absorption band disappears shortly afterward, and a new broad absorption band is detected at 366 nm with a substantially decreased extinction coefficient. The release of cytosine and protection against enzyme inactivation by reductive species are very similar to results observed with a number of substrate analogues; however, the rate of increase in absorbance at 326 nm and the subsequent decrease are considerably different from any of the previously studied compounds.^{2,21} The rate of inactivation by 2'-halo-2'-deoxynucleoside-5'-diphosphates is fast under identical conditions, and the change in absorbance on the protein at 320 nm is very slow. These results have been interpreted as indicating rapid inactivation by a nucleophilic attack of a group on the enzyme at the more reactive exocyclic methylene of 2-methylene-3(2*H*)-furanone.²⁴ The absorbance increase at 320 nm results from a subsequent attack of a lysine residue at the C1' position, ultimately leading to the putative α,β -unsaturated enamine (Scheme 1). The kinetics of the formation and the decay observed in the inhibition by *CH*₂dCDP has not yet been unravelled.

Taking into account all experimental data and earlier mechanistic studies with other 2'-substituted-nucleotide analogues, theoretical calculations on two different models of the system were performed in order to thoroughly explore the RNR:*CH*₂dCDP potential-energy surface (PES) and consequently understand the mechanism for RNR inactivation by *CH*₂dCDP. The rate of inactivation presumably can be explained by the furanone species formed.

Computational Details

Small Model. We explored the possible reactions between *CH*₂dCDP and RNR with a small model representing the active-site residues of RNR (Cys439, Cys462, Cys225, and Glu441) with *CH*₂dCDP. In this model, cysteines and glutamate residues were built as methylthiols and formate molecules, respectively. The *CH*₂dCDP molecule was modeled without the base and the diphosphate. All calculations were performed using density functional theory (DFT), with the Gaussian03 suite of programs,²⁵ at the unrestricted Becke3LYP (B3LYP) level of theory^{26–28} with the 6-31G(d) basis set. The adequacy of these models, level of theory, and basis set were demonstrated in earlier results.^{29–32} Frequency calculations confirmed the nature of each stationary point, i.e., an energy minimum with all frequencies real or, in the case of a transition state, one imaginary frequency only. The transition states were verified to connect the reactants and products of interest through internal reaction-coordinate calculations (IRC). Zero-point, thermal, and entropic effects (*T* = 298.15 K, *P* = 1 bar) were added to the calculated energies. A scale factor of 0.9804 was used to eliminate known systematic errors in zero-point energies and thermal-energy corrections. The atomic spin-density distributions were calculated by employing a Mulliken population analysis.²⁵ All optimized energies were corrected by single-point energy calculations with the 6-311++G(2d,2p) basis set and a polarized-continuum model. The polarized-continuum model, C-PCM, was employed as implemented in Gaussian03.²⁵ In this approach a continuum is modeled as a conductor instead of a dielectric. This simplifies the electrostatic computations, and corrections are made a posteriori for dielectric behavior. A dielectric constant of

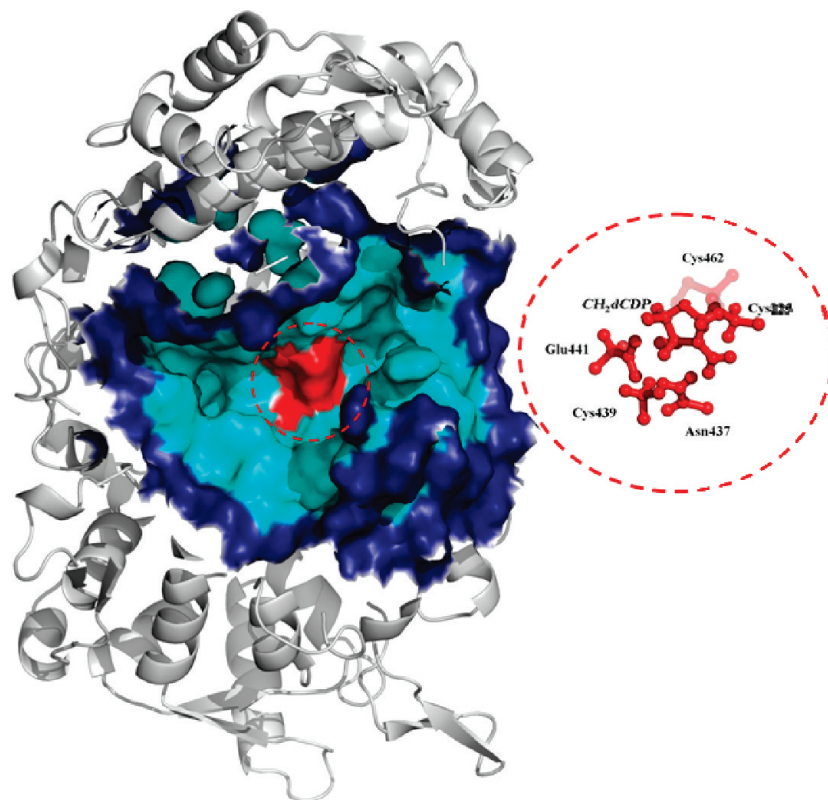


Figure 1. Representation of the enzymatic model studied, which includes a 20 Å radius of the amino acids around CH_2dCDP . The higher level region used in the QM/MM calculations is colored red, and the region treated with the lower level is colored cyan (the free region) and marine (the frozen region, the outer 5 Å shell of the entire system). The excluded part of the R1 monomer is shown in gray.

four³³ has shown previously to provide theoretical results that are in agreement with experimental results and accounts for the combined effect of the protein and buried water molecules.

Large Model. The R1 protein complexed with the inhibitor CH_2dCDP was modeled based on the crystal structure 4R1R, ribonucleotide reductase R1 protein with substrate, GDP, and effector DTTP from *E. coli*, determined by Eriksson et al.³⁴ Just one of the R1 monomers was used in the calculations. Taking into account that RNR is highly specific for ribonucleotides and they fit very tightly into the three binding pockets, (the ribose, phosphate, and base binding pockets) we created the inhibitor CH_2dCDP using the substrate as reference. The hydrogen atom and hydroxyl group that were bound to the carbon C2' of the substrate were replaced by a methylene. For the modifications we used the GaussView²⁵ software. To calculate the molecular electronic structures and properties for CH_2dCDP and DTTP we used Gaussian03,²⁵ performing restricted Hartree–Fock calculations (RHF), with the 6-31G(d) basis set, to be consistent with the parametrization adopted in Amber 8,³⁵ which was later used in the molecular mechanics calculations. We used the Antechamber tools within Amber 8, in order to create an input file for CH_2dCDP and DTTP that could be read by Leap, another of Amber's modules. Antechamber is designed to be used with GAFF, the general amber force field. RESP³⁶ was the method used to calculate atomic charges.

The R1 subunit complexed with the CH_2dCDP was minimized in order to release the bad contacts. The minimizations were performed with the parametrization adopted in Amber 8,³⁵ using the Amber force field ff99 for proteins and the Gaff force field for CH_2dCDP and DTTP.^{37–39} We solvated our complex with an octahedral box of water, using an 8 Å buffer of TIP3P water model. Our minimization procedure for solvated R1 subunit complexed with CH_2dCDP consists of a two-stage approach. In the first stage we kept the complex fixed and minimized the positions of the water and ions. Then in the second stage we minimized the entire system. About 5000 steps were used for each stage, with the first 2500 steps performed using the steepest descent algorithm and the remaining steps carried out using the conjugate gradient algorithm.

To perform the study, we used the final structure of the minimization, from which we built a model including a 20 Å radius of the enzyme around the CH_2dCDP molecule (Figure 1).

The model system was composed by a total of 6373 atoms. The QM/MM calculations performed to determine the potential-energy surface (PES) of the enzymatic model system were made with the Gaussian 03 software.²⁵ To explore the PES of the catalytic reaction, the system was divided into two layers within the ONIOM formalism^{40,41} as implemented in Gaussian 03. The higher level layer included the inhibitor without the base and the diphosphate and the side chains of the residues Cys439, Cys225, Cys462, Glu441, and Asn437 in a total of 49 atoms (Figure 1). The

higher layer was treated with density functional theory (DFT) at the unrestricted B3LYP/6-31G(d) level.^{26–28} The rest of the system was treated at the molecular mechanics level with AMBER. We have further frozen the positions of the atoms in the outer 5 Å shell of the complex (Figure 1).

For each reaction step, we performed a linear transit scan along the reaction coordinate with a step value of 0.05 Å in order to locate the geometry of the transition state. We considered the higher energy geometry as a very good approximation to the geometry of the transition state. We used the electronic embedding²⁵ scheme during the scan. Electronic embedding incorporates the partial charges of the MM region into the QM calculations and allows for polarization of the QM region by the MM charges. This technique provides a better description of the electrostatic interaction between the QM and the MM regions. The atomic spin density distributions were calculated with a Mulliken population analysis²⁵ in the higher level calculation. We calculated the energy of the optimized geometries of reactants, products, and transition states for each mechanistic step. The inclusion of diffuse functions in the basis set for geometry optimizations was investigated before and concluded that the corrections to the geometry were very small and corrections in energy differences (activation and reaction energies) were negligible.⁴² We therefore considered it unnecessary from a computational point of view to include diffuse functions in geometry optimizations, considering the inherent increase in computing time. Single-point energy calculations were then performed on the optimized geometries of the reactants, transition state, and products increasing the basis set of the higher level region to 6-311++G(2d,2p). Single-point energy calculations were also performed on all optimized geometries with the BB1K functional^{26,27,43} and two different basis sets (6-31G(d) and 6-311++G(2d,2p)). In order to understand more precisely the relative importance of long-range electrostatic/polarization effects, additional single-point energy calculations were performed on all optimized QM/MM geometries with the mechanical embedding scheme (ONIOM-ME) treating the higher level with the BB1K functional and the 6-311++G(2d,2p) basis set. ONIOM-ME neglects any polarization effects of the MM charges in the QM region.

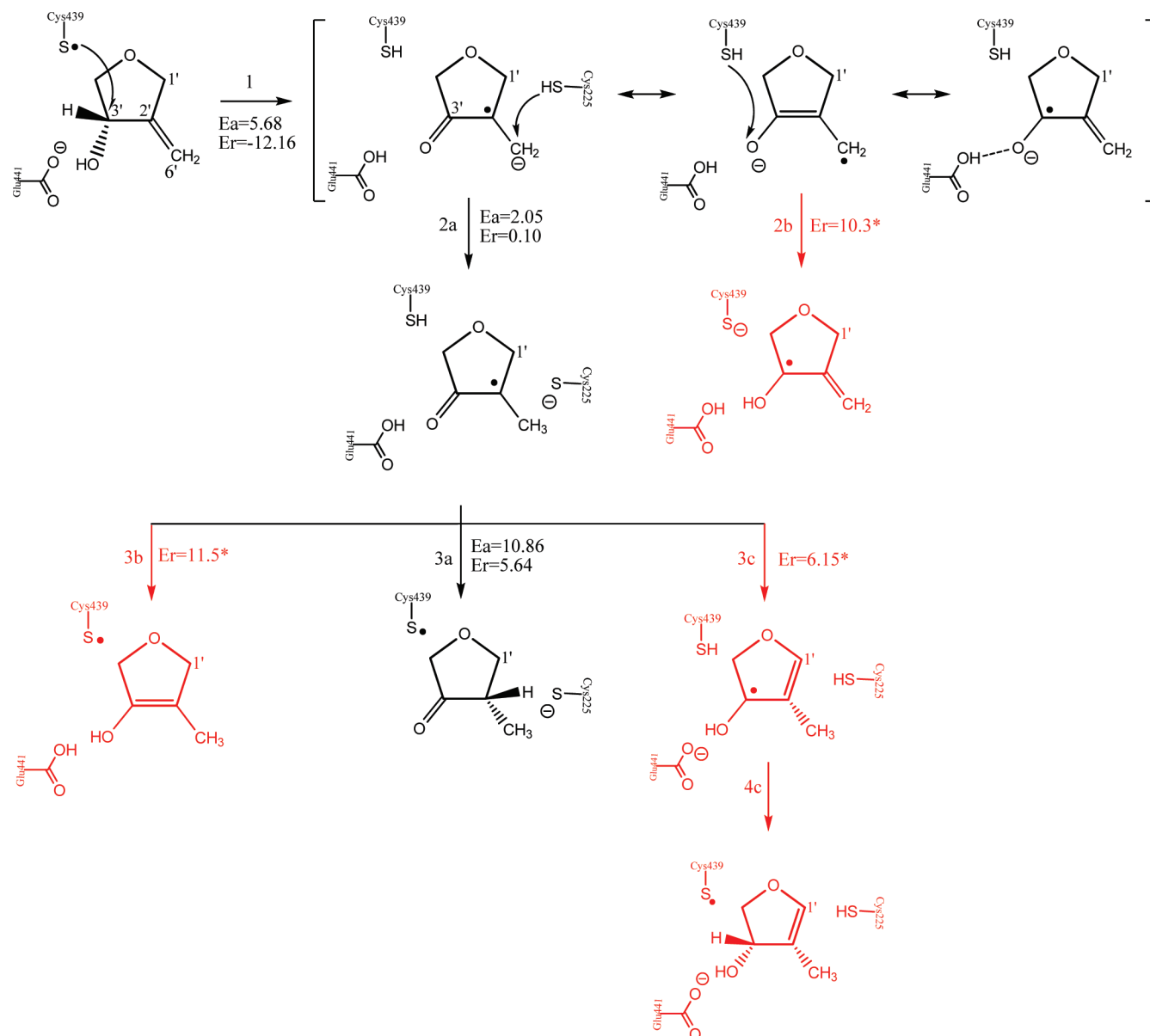
Results

Considering earlier mechanistic results with other 2'-substituted substrate analogues we tried to explore all relevant mechanistic pathways with the small model. Scheme 2 shows an overview of the reactions studied with the small model. The activation and reaction energies presented in Scheme 2 have been obtained with B3LYP using the 6-311++G(2d,2p) basis set and a polarized continuum model. Zero-point energies, thermal, and entropic effects obtained from B3LYP/6-31G(d) were added.

The first step involves abstraction of a hydrogen from carbon C3' of *CH*₂dCDP by radical Cys439 and is known to occur in the natural catalysis and with most of the substrate analogues, leading to a stable product with the spin density and the negative charge delocalized in the inhibitor and with residue Cys225 nearer to the inhibitor, more precisely closer

to the C6' carbon. The first step is very exothermic, and the reaction would be practically irreversible ($E_a = 5.68$ kcal/mol and $E_r = -12.16$ kcal/mol). The energetics of this abstraction are dissimilar to the ones obtained in an earlier study with the substrate ($E_a = 11.09$ kcal/mol, $E_r = 8.01$ kcal/mol) but more similar to that observed in earlier studies with substrate analogues, namely, a study with the substrate analogue *CHF*dCDP, which has a fluormethylene in the 2' position ($E_a = 8.01$ kcal/mol and $E_r = -7.7$ kcal/mol).⁴⁴ Taking into account the characteristics of the product of step 1 and the position of the conserved residues around, steps 2a and 2b are more promising. The product of the barrierless step 2b lies about 10 kcal/mol above the reactant and ends up falling back into it, indicating that it does not correspond to a stationary point in the potential-energy surface. There is no doubt that, out of the two, step 2a is preferential because it has a very small energy barrier ($E_a = 2.05$ kcal/mol) and is athermic ($E_r = 0.10$ kcal/mol). At this point, the inhibitor has the radical essentially located on the C3' atom and the negative charge essentially located in residue Cys225 and there are two steps that lead to regeneration of the radical sulfur of the Cys439, steps 3a and 3b, and one step, step 3c, which seems relevant due to the proximity between carbon C1' of the inhibitor and residue Cys225. The products of steps 3b and 3c do not correspond to stationary points on the potential-energy surface, and they fall back into the reactant. It seems logical that step 3c is unfavorable comparatively with step 3a; however, we decided to confirm with the larger model because the energy required to form the unstable compound is not very high and step 4c probably could stabilize it. The reactions (steps 1, 2a, 3a, and 3c) were tested with the larger model. The larger model allowed us to discard step 3c beyond any doubt; the energy barrier obtained for this step (more than 35 kcal/mol) is too high to match experimental kinetics. The large difference between the small and large model is unique in this step. This is due to the large stereochemical constraints imposed by the protein for Cys225 to reach C1. In the small model those constraints are absent. No other step is expected to exhibit a similar difference between models. We note that each transition state of each step is characterized by a unique imaginary frequency, specifically, 1291i cm⁻¹ for step 1, 725.3i cm⁻¹ for step 2a, and 1072i cm⁻¹ for step 3a. Finally, the more viable mechanism is shown in detail (Scheme 3).

For the sake of comparing mechanisms B3LYP is a very efficient tool. It is much faster and has better convergence properties than the modern hybrid-meta functionals, two requisites very helpful to explore mechanistic pathways. However, to obtain final values for the PES we preferred to use the BB1K energies, and these are the ones which will be discussed above. BB1K has been shown to significantly outdo B3LYP in several properties, namely, provide more realistic barriers. We also calculated the B3LYP energies for the large model in the preferred pathway and confirmed that in all reactions the activation energies provided by B3LYP (Supporting Information) were up to 1.0–4.5 kcal/mol smaller than the BB1K values. Each mechanistic step will be discussed, presenting the results obtained with the larger model that provides further insights and efficiently

Scheme 2. Overview of the Relevant Reactions Explored with the Small Model in Order To Unravel the Mechanism for RNR Inhibition by CH_2dCDP^a 

^a All energy values are in kcal/mol. The asterisk (*) identifies the cases for which the energy of the products do not correspond to a stationary point in the potential-energy surface but represents the higher energy value of the scan.

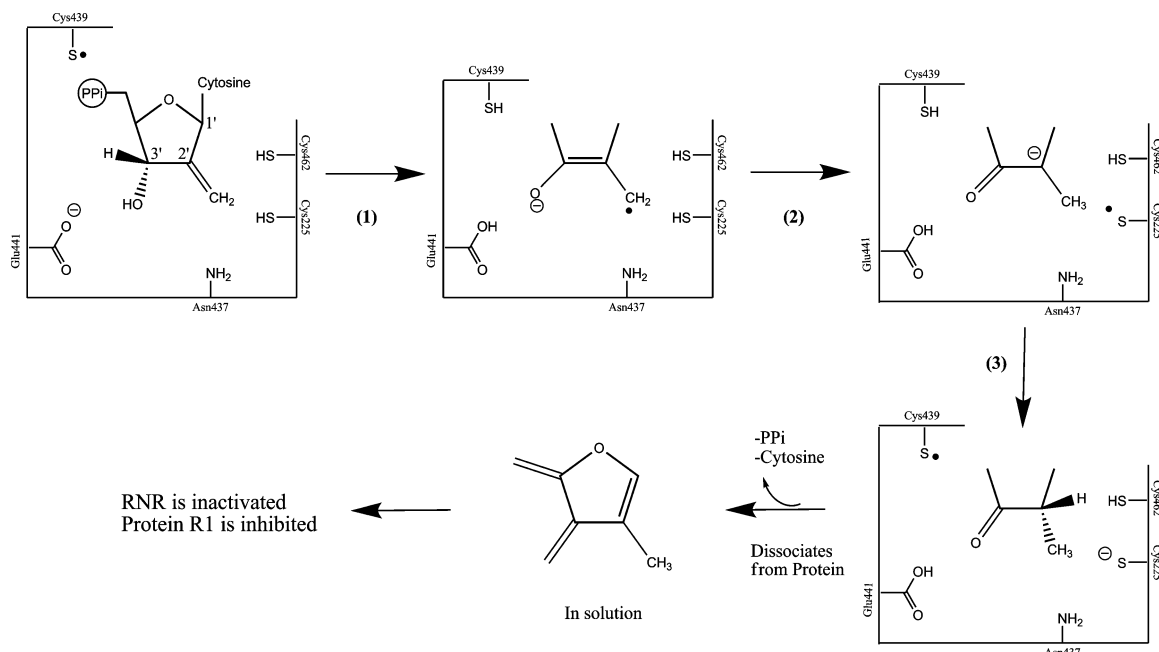
account for the long-range RNR- CH_2dCDP interactions and stereochemical strain imposed by the protein scaffold. In order to calculate the activation and reaction energies, the energy of each state has been calculated as the energy obtained with ONIOM (using BB1K/6-311++G(2d,2p) for the higher layer and AMBER for the rest of the system), corrected by zero-point energy, thermal, and entropic effects (eq 1).

$$E = E_{\text{ONIOM(B3LYP/6-311++G(2d,2p)//AMBER)}} + (\text{ZPE} + \text{thermal} + \text{entropic})_{\text{B3LYP/6-31G(d)}} \quad (1)$$

First Mechanistic Step. The first step involves abstraction of a hydrogen from carbon $C3'$ of CH_2dCDP by radical Cys439 previously formed, as observed with the natural

substrate and with some substrate analogues previously studied. Similarly, one proton of the hydroxyl group connected to the $C3'$ of the inhibitor ($HO-C3'$) migrates to residue Glu441 spontaneously. This rearrangement of the system is energetically and thermodynamically favorable, the calculated free energy barrier necessary to achieve the transition state is 6.39 kcal/mol, and the reaction free energy is -22.08 kcal/mol.

In the reactants, the thiyl atom of Cys439, where the spin density is located (0.91 au), is found at 2.60 Å from the hydrogen that is bound to the $C3'$ carbon ($H-C3'$) and the proton atom of the hydroxyl group connected to the $C3'$ ($HO-C3'$) is at 1.60 Å from the oxygen atom of the Glu441. Figure 2 represents the geometry of the transition state. At this point the hydrogen is located 1.65 Å away from the

Scheme 3. Proposed Mechanism for RNR Inhibition by CH_2dCDP 

sulfur (Cys439) and 1.32 Å from the carbon C3' of the inhibitor. The proton of the HO-C3' group is in an almost perfectly collinear fashion with the oxygen atom of the Glu441 with an O-H-O angle of 177.5° and is still closer to the O-C3' bond (1.10 Å from the oxygen atom that is bound to the C3' carbon and 1.40 Å from the oxygen of the Glu441). The C3'-O and C3'-C2' bonds are 0.05 and 0.06 Å shorter than in the reactants, and the C3'-C6' bond is 0.10 Å elongated. In the optimized geometry of the products the C3'-O and C3'-C2' bonds are further shortened to 1.30 and 1.41 Å, respectively, and the C3'-C6' bond is more elongated to 1.38 Å. The spin density is essentially located in the C6' atom (0.61 au) but delocalized to the carbon C3' (0.36 au), and the negative charge of the system becomes localized in the inhibitor because Glu441 is now protonated.

Second Mechanistic Step. At the end of step 1, the C2'-C6' bond has become elongated and the spin density is essentially located in the C6' atom, revealing that C6' can easily receive one hydrogen. The hydrogen atom of Cys225 is distanced by 2.43 Å from the C6' atom of the inhibitor. The second step consists of the transfer of a hydrogen from Cys225 to the carbon C6' of the inhibitor. The transition state for reaction 2 is represented in Figure 3.

At this point the hydrogen is shared between the sulfur (1.62 Å) of Cys225 and the carbon C6' of the inhibitor (1.45 Å). The distance C2'-C6' is further elongated to 1.42 Å, and the spin density is essentially in carbon C6' (0.36 au) and in the sulfur atom of residue Cys225 (0.28 au). In the optimized structure of the products, the sulfur atom of

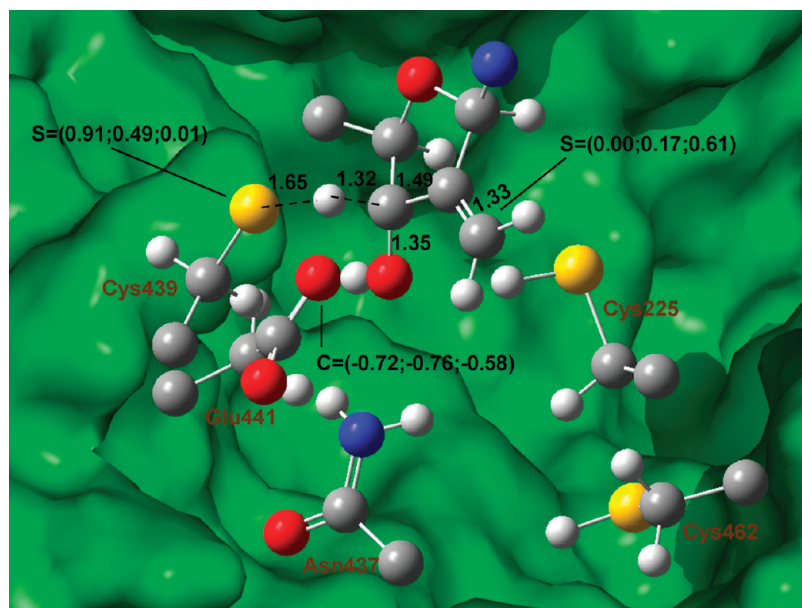


Figure 2. Geometry of transition state 1 labeled with relevant bond lengths (in Angstroms), spin density distribution (S) in au, and the charges (C) of the three geometries (reactants, transition state, and products).

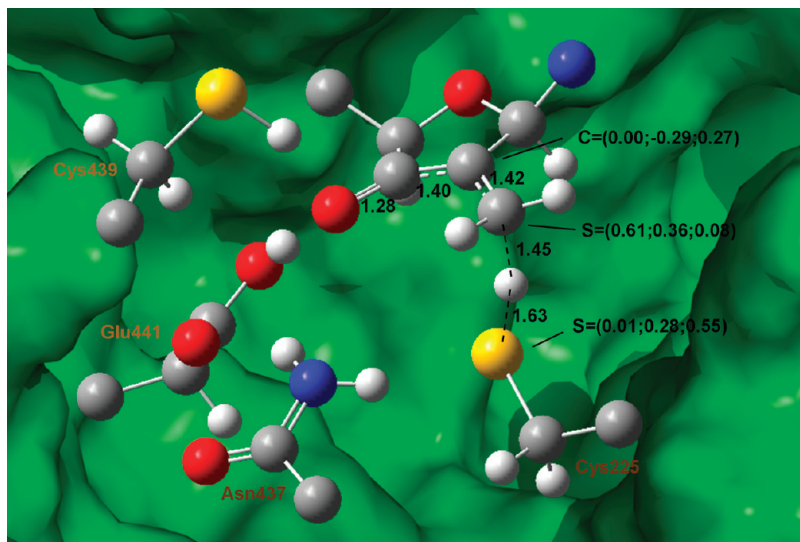


Figure 3. Geometry of transition-state 2 labeled with relevant bond lengths (in Angstroms), spin density distribution (S) in au, and charges (C) of the three geometries (reactants, transition state, and products).

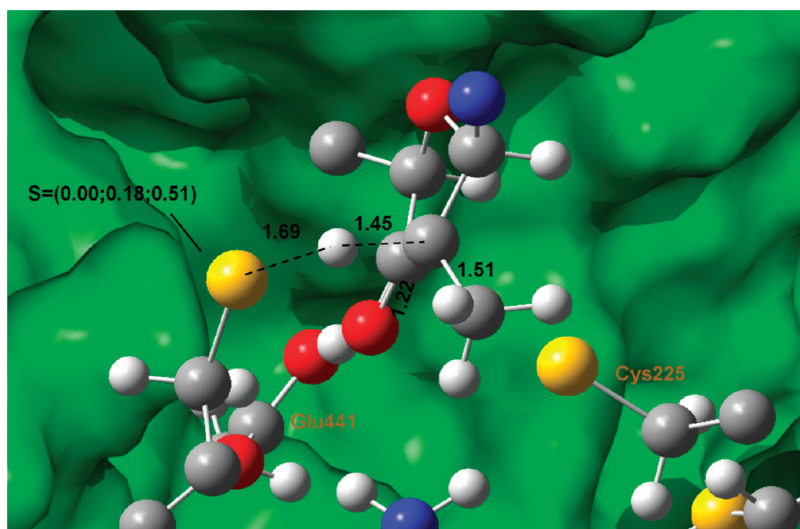


Figure 4. Geometry of transition-state 3 labeled with relevant bond lengths (in Angstroms), spin density distribution (S) in au, and the charges (C) of the three geometries (reactants, transition state, and products).

Cys225 is 2.43 Å away from the hydrogen, the C6'–C2' bond is 1.47 Å and the C2'–C3' and C3'–O bonds are shorter (1.38 and 1.29 Å, respectively). The spin density is mainly located at the sulfur atom of the Cys225 (0.55 au), although it is still delocalized to carbon C2'. As a consequence of resonance, the negative charge is delocalized between the C2' of the inhibitor and the oxygen atom that is bound to the C3'. The calculated free energy barrier necessary to achieve the transition state is 10.05 kcal/mol, and the reaction free energy is 8.27 kcal/mol.

Third Mechanistic Step. At this point of the reaction pathway, there is clearly one step that would lead to regeneration of the R1 radical. It consists in the donation of the thiol hydrogen of Cys439 to carbon C2'. In the optimized structure of the reactants, the hydrogen of Cys439 is distanced by 3.37 Å to the C2' carbon of the inhibitor. The activation free energy for this reaction is 16.70 kcal/mol, and the reaction free energy is 3.87 kcal/mol. Figure 4 depicts the geometry of the transition state, where the hydrogen is

1.64 Å away from the sulfur atom of Cys439 and 1.45 Å from the carbon C2' at an angle of 174.7°.

In the optimized structure of the products the sulfur atom of Cys439 is 2.43 Å away from the hydrogen, the C6'–C2' bond length is 1.53 Å, C2'–C3' is 1.51 Å, and C3'–O is 1.22 Å. The spin density is essentially in the sulfur atom of the Cys439 (0.51 au), and the negative charge is essentially in the sulfur atom of the Cys225. This way, the initial thiyl radical is regenerated and a 2'-methyl-3'-ketodeoxyribonucleotide is formed. This step has the higher activation energy (also in small model). It must be noted that a barrier of 15.64 kcal/mol is in agreement with the experimental kinetics for this reaction (the barrier for the limiting step is less than 20 kcal/mol).²⁴

RNR Inhibition. According to experimental results, the 2'-methyl-3'-ketodeoxyribonucleotide does not remain attached to the active site and has a propensity to dissociate to the solvent. Once in solution, the 2'-methyl-3'-ketodeoxyribonucleotide loses the base and the phosphate groups and

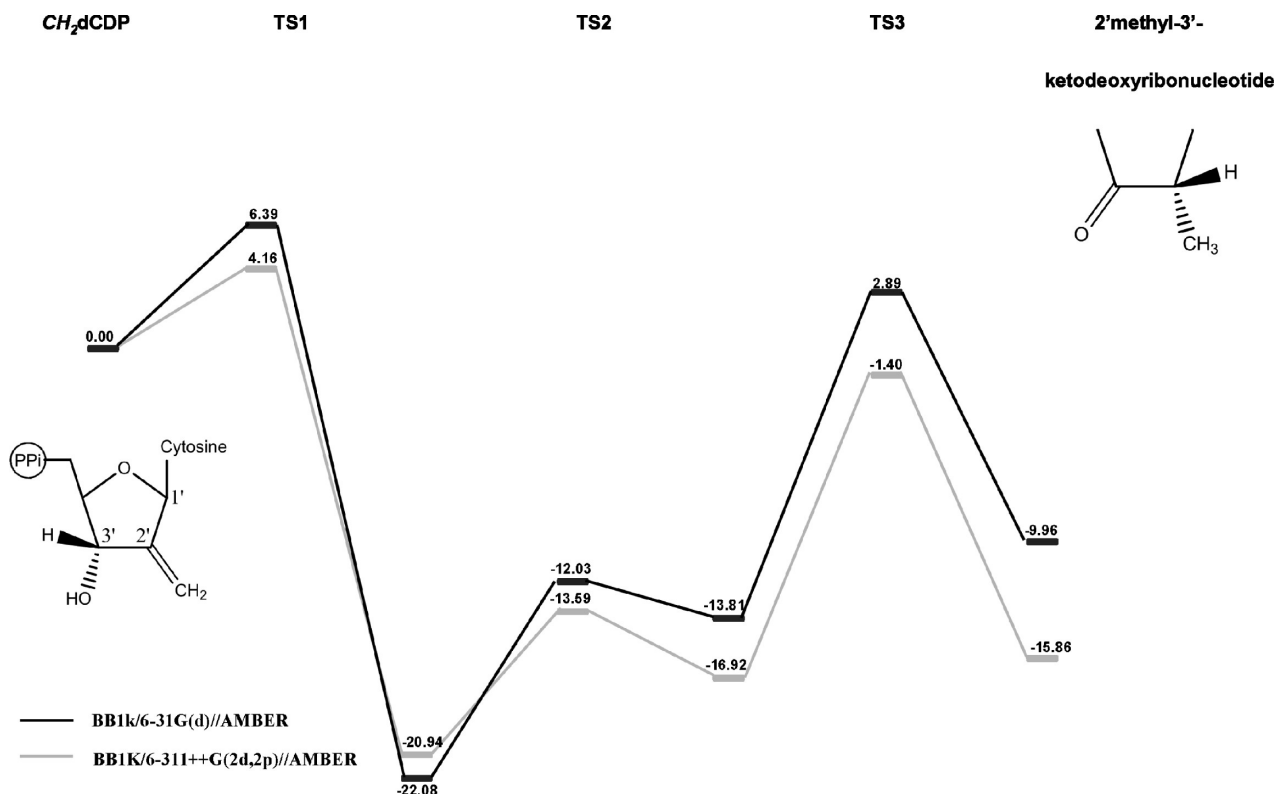


Figure 5. Energetic profile of the mechanism proposed for the RNR interaction with CH_2dCDP .

generates a methylfuranone derivative (Scheme 3). Subsequently, this compound inhibits subunit R1, forming a chromophore with a characteristic absorption band at 326 nm. This seems to be consistent with production of a methyl-substituted α,β -unsaturated enamine by analogy with 2'-halo-2'-deoxynucleoside-5'-diphosphates chemistry (Scheme 1). Replacement of H by CH_3 in the furanone would be expected to red shift the wavelength λ by 5–10 nm.²¹ What is atypical is that the rate of appearance of λ at 326 nm is fast and similar to the rate of inactivation. The rate of inactivation by 2'-halo-2'-deoxynucleoside-5'-diphosphates is fast, and the change in absorbance on the protein at 320 nm is very slow. Probably, the presence of a methyl group bound to the C2' atom would conduct a faster attack of a lysine residue at the C1' position. We searched hard, computationally, but have not found another favorable pathway that would lead to a second chemical species besides the above-mentioned furanone and consequently justify the second absorption value at 366 nm. However, since the absorbance at 326 nm disappears completely and a new absorption band is formed, subsequent chemical rearrangements within the R1 active site might explain this observation. In fact, formation of a single methylfuranone and its subsequent rearrangement would be in agreement with the experimental findings. These rearrangements might be due to a different binding pose/ binding location due to the extra methyl group.

Overall Reaction Energy. In Figure 5 we present the overall energetic profile of the mechanism proposed for the RNR interaction with CH_2dCDP now calculated with the more accurate and time-extensive BB1K density functional.

According to Figure 5, the mechanism proposed for RNR inhibition has an overall reaction energy of -15.86 and

-9.96 kcal/mol using the functional BB1K with 6-31G(d) and 6-311++G(2d,2p), respectively, and is therefore thermodynamically favored. We note the functional BB1K overestimates slightly (~ 1 kcal/mol) the energy for the generality of the theoretical studies made with different enzymes.⁴⁵ When comparing the basis sets the activation and reaction energies have augmented in all steps except the first. This would be expected since all steps involve transfer of hydrogens or protons. The first mechanistic step is the most favorable thermodynamically, and the third step is the limiting one, with the higher activation barrier. Note that the overall PES is slightly endothermic after step 1, which would suggest that the reaction could be trapped in the first intermediate. The thermodynamic driving force for the inhibition comes from the very exothermic dissociation of the 2'methyl-3'-ketodeoxyribonucleotide to solution,⁴⁶ which makes the overall process very favorable. There is no doubt that computationally this is the most viable mechanistic pathway.

Electrostatic/Polarization and Strain at the Active Site. In the proposed mechanism for RNR interaction with CH_2dCDP the ONIOM-EE calculations were used to take into account the long-range interactions, the stereochemical strain imposed by the protein scaffold, and the polarization/electrostatic effect on the QM layer due to the MM layer. In this subsection of the results we comment more precisely on the relative importance of the long-range electrostatic/polarization and stereochemical strain.

To calculate the contribution of the stereochemical strain for the activation and reaction energies we compared the energies of the small free system in the gas phase (ΔE^{free}) with the energies of that same system also in the gas phase

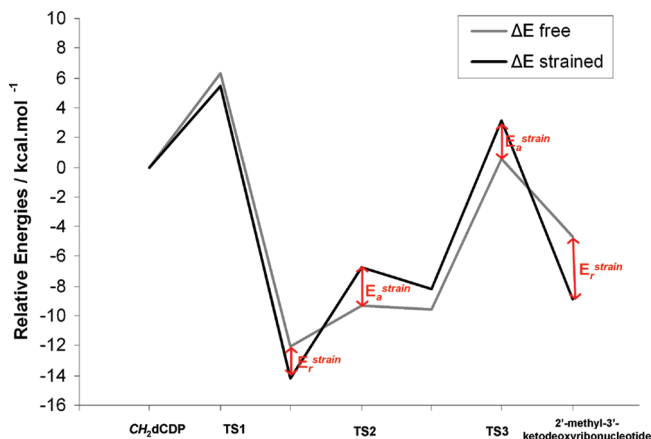


Figure 6. Stereochemical strain contribution for the energy profile.

but with the precise geometry obtained in the full QM/MM model ($\Delta E^{\text{strained}}$). The energies were recalculated to eliminate the effects of the dielectric continuum for the first case and the polarization by the MM region in the second case. The strain contribution for the activation energy ($E_a^{\text{strain}} = \Delta E_a^{\text{strained}} - \Delta E_a^{\text{free}}$) and for the reaction energy ($E_r^{\text{strain}} = \Delta E_r^{\text{strained}} - \Delta E_r^{\text{free}}$) are shown in Figure 6. We note that the driving force that leads to the strained geometry in the QM/MM model is not only the “mechanical strain” imposed by the almost rigid bonds and angles that connect the residues to the backbone but also the electrostatic field created by the remaining protein scaffold. It is obvious that most of the contribution comes from the mechanical strain.

In Figure 6 we can see that the strain energy favors transition-state 1 (TS1) and product 1 (P1), with $E_a^{\text{strain}} = -0.91$ kcal/mol and $E_r^{\text{strain}} = -2.17$ kcal/mol. Strain facilitates the first step. The constraints of the position/orientation of the CH_2dCDP and the reactive-site residues due to their connections to protein scaffold disfavors generation of TS2 and TS3 (E_a^{strain} is ~ 2.5 kcal/mol in both) and P2 ($E_r^{\text{strain}} = 1.37$ kcal/mol). The strain contribution for the overall reaction energy is -4.24 kcal/mol, i.e., the strain due to the protein scaffold favors formation of the 2'-methyl-3'-ketodeoxyribonucleotide. Looking to the overall energetic profile we can see that the constraints imposed by the protein scaffold play a minimal catalyst role in the catalytic mechanism. This is one more argument that supports the

previous use of cluster models in studies of the catalytic mechanism of RNR.^{31,42,47}

An interesting technical issue is the extent to which the electronic polarization of the substrate and active site contributes to the potential-energy profile. The polarization always increases the electronic energy when compared to the gas-phase unpolarized system. However, this energetic cost must be compensated by the increased electrostatic interactions between the polarizing (MM layer) and polarized (QM layer) regions. The contribution of the polarization energy to the activation energy (E_a^{pol}) and reaction energy (E_r^{pol}) is given by the differences in the high-level layer PES calculated with ONIOM-EE and ONIOM-ME ($E_a^{\text{pol}} = \Delta E_a^{\text{high, ONIOM-EE}} - \Delta E_a^{\text{high, ONIOM-ME}}$ and $E_r^{\text{pol}} = \Delta E_r^{\text{high, ONIOM-EE}} - \Delta E_r^{\text{high, ONIOM-ME}}$), always using the same ONIOM-EE geometries. See Figure 7.

The contribution of the polarization energy to TS1 is negligible ($E_a^{\text{pol}} = 0.05$ kcal/mol). Polarization becomes in fact significant after the first step. The long-range polarization effects disfavor TS2 ($E_r^{\text{pol}} = 9.01$ kcal/mol) and favors to a great extent P2, TS3, and the final product. The polarization contribution for the overall reaction energy is -17.25 kcal/mol, extensively favoring formation of the final product 2'-methyl-3'-ketodeoxyribonucleotide. The polarization effect has an important contribution to the stabilization, favoring quantitatively the products of the proposed mechanism. However, analyzing the high-layer polarization effects alone may be misleading, as polarization gives rise to enhanced electrostatic interactions with the MM region, and these two effects should be analyzed together. The enzyme rotameric response to the field created by the substrate is only poorly measured, even in long MD simulations. Atomic polarization at the MM layer is also not explicitly accounted for with the usual biomolecular force fields. The most straightforward way to account for polarization and electrostatic effects together is to compare the results obtained with the electronic embedding and mechanical embedding schemes. We have done so for the first step of the reaction, as an example. However, there is a strong bias in the process, which is the fact that the mechanical embedding results depend on the atomic point charges used to parametrize the MM region. Point charges are usually first calculated by fitting to the QM electrostatic potential (conventional point charges) and

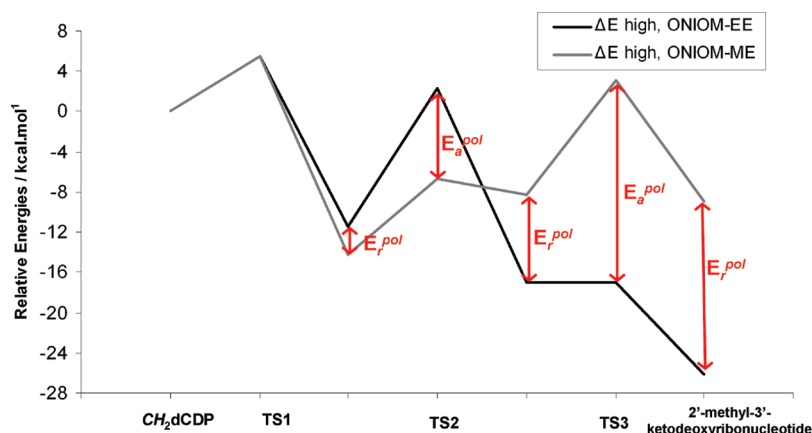


Figure 7. Polarization contribution for the energy profile.

then empirically adjusting to reproduce known data (effective point charges) to overcome limitations inherent to the fitting process and lack of MM atomic polarization. However, the only reference we have is the electronic embedding result, and to fit the charges to reproduce the electronic embedding result would make the assessment of polarization/electrostatic effects biased and meaningless. Therefore we used just conventional point charges (both Mulliken charges and HF/6-31G(d) ESP fit charges) to recalculate the energy of the first step with mechanical embedding. The results for the first step were $E_a = 12.9$ kcal/mol and $E_r = -22.7$ kcal/mol with Mulliken charges and $E_a = 24.0$ kcal/mol and $E_r = -4.56$ kcal/mol with HF/6-31G(d) ESP fit charges, which clearly shows that the results of mechanical embedding are very much dependent on the scheme used to generate point charges and not very reliable (if electrostatic embedding is taken as a reference) unless one has a way to empirically adjust the point charges of the MM layer. Note that inclusion of ESP charges derived from the electrostatic embedding electronic density (i.e., “polarized point charges”) followed by MM geometry reoptimization led to very similar results to the ones obtained with the ESP “unpolarized” charges, which highlights the importance of the parametrization of the QM regions and the dependence of the results on this process. We consider it to be preferable to use electronic embedding as it is more objective and less dependent on the exact choice of the method/protocol to parametrize the high layer.

Conclusions

This study has allowed for comprehension of the mechanism in which 2'-deoxy-2'-methylenecytidine-5'-diphosphate inhibits RNR, with atomistic detail. Even though this work was derived from theoretical calculations, all earlier experimental results were taken into account. We propose the more viable mechanistic pathway for RNR inactivation by CH_2dCDP in three steps. The first mechanistic step involves abstraction of a hydrogen from carbon C3' of CH_2dCDP by radical Cys439. In fact and spontaneously, one proton of the hydroxyl group connected to the C3' carbon atom of the inhibitor migrates to Glu441. The second step consists of transfer of a hydrogen from Cys225 to the carbon C6' of the inhibitor. The third step consists of donation of the thiol hydrogen of Cys439 to carbon C2'. The 2'-methyl-3'-ketodeoxyribonucleotide formed does not remain attached to the active site, dissociating instead to the solvent. Once in the solvent, it loses the base and the phosphate groups and generates a methylfuranone derivative. The methylfuranone derivative inhibits subunit R1. Probably, the presence of a methyl group bound to the C2' carbon atom will conduct to a faster attack of a lysine residue at the C1' position inside the R1 subunit active site, leading to a fast rate of appearance of λ at 326 nm. The single methylfuranone formed in all probability explains the second absorption value detected at 366 nm by chemically rearranging within the R1 active site, probably due to a different binding pose/site caused by the presence of the methyl group in the furanone species. This event would explain the complete disappearance of the

absorption value at 326 nm and formation of a new absorption band at 366 nm.

Acknowledgment. M.A.S.P. would like to thank the Fundação para a Ciência e a Tecnologia (FCT) for a Ph.D. grant.

Supporting Information Available: Energies of the reactants, transition states and products, provided by B3LYP (and BB1K) using the large model, are presented in the Supporting Information. The coordinates (together with charges, layers and connectivities) of each reactant, transition state and product are also presented in the Supporting Information. This material is available free of charge via the Internet at <http://pubs.acs.org>.

References

- (1) Lawrence, C. C.; Bennati, M.; Obias, H. V.; Bar, G.; Griffin, R. G.; Stubbe, J. High-field EPR detection of a disulfide radical anion in the reduction of cytidine 5'-diphosphate by the E441Q R1 mutant of *Escherichia coli* ribonucleotide reductase. *Proc. Natl. Acad. Sci. U.S.A.* **1999**, *96*, 8979–8984.
- (2) Robins, M. J.; Samano, V.; Zhang, W. J.; Balzarini, J.; Declercq, E.; Borchardt, R. T.; Lee, Y.; Yuan, C. S. Nucleic-Acid Related-Compounds 0.74. Synthesis and Biological-Activity of 2'(and 3')-Deoxy-2'(and 3')-Methylenenucleoside Analogs That Function as Mechanism-Based Inhibitors of S-Adenosyl-L-Homocysteine Hydrolase and or Ribonucleotide Reductase. *J. Med. Chem.* **1992**, *35*, 2283–2293.
- (3) Stubbe, J. A.; van der Donk, W. A. Ribonucleotide reductases: Radical enzymes with suicidal tendencies. *Chem. Biol.* **1995**, *2*, 793–801.
- (4) Cory, J. G. Ribonucleotide Reductase as a Chemotherapeutic Target. *Adv. Enzyme Regul.* **1988**, *27*, 437–455.
- (5) Nocentini, G. Ribonucleotide reductase inhibitors: New strategies for cancer chemotherapy. *Crit. Rev. Oncol./Hematol.* **1996**, *22*, 89–126.
- (6) Gerfen, G. J.; van der Donk, W. A.; Yu, G. X.; McCarthy, J. R.; Jarvi, E. T.; Matthews, D. P.; Farrar, C.; Griffin, R. G.; Stubbe, J. Characterization of a substrate-derived radical detected during the inactivation of ribonucleotide reductase from *Escherichia coli* by 2'-fluoromethylene-2'-deoxycytidine 5'-diphosphate. *J. Am. Chem. Soc.* **1998**, *120*, 3823–3835.
- (7) Zhou, B. B. S.; Elledge, S. J. The DNA damage response: putting checkpoints in perspective. *Nature* **2000**, *408*, 433–439.
- (8) Eklund, H.; Uhlin, U.; Farnegardh, M.; Logan, D. T.; Nordlund, P. Structure and function of the radical enzyme ribonucleotide reductase. *Prog. Biophys. Mol. Biol.* **2001**, *77*, 177–268.
- (9) Stubbe, J. A.; van der Donk, W. A. Protein radicals in enzyme catalysis (vol 98, pg 705, 1998). *Chem. Rev.* **1998**, *98*, 705–762.
- (10) Scott, C. P.; Kashlan, O. B.; Lear, J. D.; Cooperman, B. S. A quantitative model for allosteric control of purine reduction by murine ribonucleotide reductase. *Biochemistry* **2001**, *40*, 1651–1661.
- (11) Kashlan, O. B.; Scott, C. P.; Lear, J. D.; Cooperman, B. S. A comprehensive model for the allosteric regulation of mam-

- malian ribonucleotide reductase. Functional consequences of ATP- and dATP-induced oligomerization of the large subunit. *Biochemistry* **2002**, *41*, 462–474.
- (12) Barlow, T. Evidence for a New Ribonucleotide Reductase in Anaerobic Escherichia-Coli. *Biochem. Biophys. Res. Commun.* **1988**, *155*, 747–753.
 - (13) Fontecave, M.; Eliasson, R.; Reichard, P. Oxygen-Sensitive Ribonucleoside Triphosphate Reductase Is Present in Anaerobic Escherichia-Coli. *Proc. Natl. Acad. Sci. U.S.A.* **1989**, *86*, 2147–2151.
 - (14) van der Donk, W. A.; Yu, G. X.; Perez, L.; Sanchez, R. J.; Stubbe, J.; Samano, V.; Robins, M. J. Detection of a new substrate-derived radical during inactivation of ribonucleotide reductase from Escherichia coli by gemcitabine 5'-diphosphate. *Biochemistry* **1998**, *37*, 6419–6426.
 - (15) Mohr, M.; Zipse, H. C-H bond activation in ribonucleotide reductases - Do short, strong hydrogen bonds play a role. *Chem.—Eur. J.* **1999**, *5*, 3046–3054.
 - (16) Stubbe, J.; Yee, C. S.; Chang, M. C. Y.; Ge, J.; Nocera, D. G. Ribonucleotide reductase: Unnatural amino acids to probe proton coupled electron transfer. *Abstr. Pap. Am. Chem. Soc.* **2003**, *226*, 054-BIOL.
 - (17) Stubbe, J. Radicals with a controlled lifestyle. *Chem. Commun.* **2003**, 2511–2513.
 - (18) Zipse, H. The influence of hydrogen bonding interactions on the C-H bond activation step in class I ribonucleotide reductases. *Org. Biomol. Chem.* **2003**, *1*, 692–699.
 - (19) Bennati, M.; Robblee, J. H.; Mugnaini, V.; Stubbe, J.; Freed, J. H.; Borbat, P. EPR distance measurements support a model for long-range radical initiation in E.coli ribonucleotide reductase. *J. Am. Chem. Soc.* **2005**, *127*, 15014–15015.
 - (20) Strand, K. R.; Karlsen, S.; Kolberg, M.; Rohr, A. K.; Gorbitz, C. H.; Andersson, K. K. Crystal structural studies of changes in the native dinuclear iron center of ribonucleotide reductase protein R2 from mouse. *J. Biol. Chem.* **2004**, *279*, 46794–46801.
 - (21) Baker, C. H.; Banzon, J.; Bollinger, J. M.; Stubbe, J.; Samano, V.; Robins, M. J.; Lippert, B.; Jarvi, E.; Resvick, R. 2'-Deoxy-2'-Methylenecytidine and 2'-Deoxy-2',2'-Difluorocytidine 5'-Diphosphates - Potent Mechanism-Based Inhibitors of Ribonucleotide Reductase. *J. Med. Chem.* **1991**, *34*, 1879–1884.
 - (22) Takenuki, K.; Matsuda, A.; Ueda, T.; Sasaki, T.; Fujii, A.; Yamagami, K. Nucleosides and Nucleotides 0.83. Design, Synthesis, and Antineoplastic Activity of 2'-Deoxy-2'-Methylenecytidine. *J. Med. Chem.* **1988**, *31*, 1063–1064.
 - (23) Masuda, N.; Matsui, K.; Yamamoto, N.; Nogami, T.; Nakagawa, K.; Negoro, S.; Takeda, K.; Takifuji, N.; Yamada, M.; Kudoh, S.; Okuda, T.; Nemoto, S.; Ogawa, K.; Myobudani, H.; Nihira, S.; Fukuoka, M. Phase I trial of oral 2'-deoxy-2'-methylenecytidine: On a daily x 14-day schedule. *Clin. Cancer Res.* **2000**, *6*, 2288–2294.
 - (24) Baker, C.; Banzon, J.; Bollinger, J.; Stubbe, J.; Samano, V.; Robins, M.; Lippert, B.; Jarvi, E.; Resvick, R. 2'-Deoxy-2'-Methylenecytidine and 2'-Deoxy-2',2'-Difluorocytidine 5'-Diphosphates - Potent Mechanism-Based Inhibitors of Ribonucleotide Reductase. *J. Med. Chem.* **1991**, *34*, 1879–1884.
 - (25) Trucks, R. C.; M. J. F.; G. W. Schlegel, H. B. Scuseria, G. E. Robb, M. A. Cheeseman, J. R. Montgomery, J. A., Jr., Vreven, T. Kudin, K. N. Burant, J. C. Millam, J. M. Iyengar, S. S. Tomasi, J. Barone, V. Mennucci, B. Cossi, M. Scalmani, G. Rega, N. Petersson, G. A. Nakatsuji, H. Hada, M. Ehara, M. Toyota, K. Fukuda, R. Hasegawa, J. Ishida, M. Nakajima, T. Honda, Y. Kitao, O. Nakai, H. Klene, M. Li, X. Knox, J. E. Hratchian, H. P. Cross, J. B. Bakken, V. Adamo, C. Jaramillo, J. Gomperts, R. Stratmann, R. E. Yazyev, O. Austin, A. J. Cammi, R. Pomelli, C. Ochterski, J. W. Ayala, P. Y. Morokuma, K. Voth, G. A. Salvador, P. Dannenberg, J. J. Zakrzewski, V. G. Dapprich, S. Daniels, A. D. Strain, M. C. Farkas, O. Malick, D. K. Rabuck, A. D. Raghavachari, K. Foresman, J. B. Ortiz, J. V. Cui, Q. Baboul, A. G. Clifford, S. Cioslowski, J. Stefanov, B. B. Liu, G. Liashenko, A. Piskorz, P. Komaromi, I. Martin, R. L. Fox, D. J. Keith, T. Al-Laham, M. A. Peng, C. Y. Nanayakkara, A. Challacombe, M. Gill, P. M. W. Johnson, B. Chen, W. Wong, M. W. Gonzalez, and C. Pople, J. A. *Gaussian 03*; Gaussian, Inc.: Wallingford, CT, 2004.
 - (26) Becke, A. D. Density-Functional Exchange-Energy Approximation with Correct Asymptotic-Behavior. *Phys. Rev. A* **1988**, *38*, 3098–3100.
 - (27) Becke, A. D. Density-functional thermochemistry 0.4. A new dynamical correlation functional and implications for exact-exchange mixing. *J. Chem. Phys.* **1996**, *104*, 1040–1046.
 - (28) Lee, C. T.; Yang, W. T.; Parr, R. G. Development of the Colle-Salvetti Correlation-Energy Formula into a Functional of the Electron-Density. *Phys. Rev. B* **1988**, *37*, 785–789.
 - (29) Himo, F. Quantum chemical modeling of enzyme active sites and reaction mechanisms. *Theor. Chem. Acc.* **2006**, *116*, 232–240.
 - (30) Cerqueira, N.; Fernandes, P. A.; Eriksson, L. A.; Ramos, M. J. Dehydration of ribonucleotides catalyzed by ribonucleotide reductase: The role of the enzyme. *Biophys. J.* **2006**, *90*, 2109–2119.
 - (31) Cerqueira, N.; Fernandes, P. A.; Ramos, M. L. Understanding ribonucleotide reductase inactivation by gemcitabine. *Chem.—Eur. J.* **2007**, *13*, 8507–8515.
 - (32) Leopoldini, M.; Marino, T.; Michelini, M. D.; Rivalta, I.; Russo, N.; Sicilia, E.; Toscano, M. The role of quantum chemistry in the elucidation of the elementary mechanisms of catalytic processes: from atoms, to surfaces, to enzymes. *Theor. Chem. Acc.* **2007**, *117*, 765–779.
 - (33) Siegbahn, P. E. M.; Eriksson, L.; Himo, F.; Pavlov, M. Hydrogen atom transfer in ribonucleotide reductase (RNR). *J. Phys. Chem. B* **1998**, *102*, 10622–10629.
 - (34) Eriksson, M.; Uhlin, U.; Ramaswamy, S.; Ekberg, M.; Regnstrom, K.; Sjoberg, B.; Eklund, H. Binding of allosteric effectors to ribonucleotide reductase protein R1: reduction of active-site cysteines promotes substrate binding. *Structure* **1997**, *5*, 1077–1092.
 - (35) Case, D. A.; Darden, T. A.; Cheatham, T. E., III; Simmerling, C. L.; Wang, J.; Duke, R. E.; Luo, R.; Merz, H. M.; Wang, B.; Pearlman, D. A.; Crowley, M.; Brozell, S.; Tsui, V.; Gohlke, H.; Mongan, J.; Hornak, V.; Cui, G.; Beroza, P.; Schafmeister, C.; Caldwell, J. W.; Ross, W. S.; Kollman, P. A. *AMBER 8*; University of California: San Francisco, CA, 2004.
 - (36) Bayly, C. I.; Cieplak, P.; Cornell, W. D.; Kollman, P. A. A Well-Behaved Electrostatic Potential Based Method Using Charge Restraints for Deriving Atomic Charges - the Resp Model. *J. Phys. Chem.* **1993**, *97*, 10269–10280.
 - (37) Basma, M.; Sundara, S.; Calgan, D.; Vernali, T.; Woods, R. J. Solvated ensemble averaging in the calculation of partial atomic charges. *J. Comput. Chem.* **2001**, *22*, 1125–1137.

- (38) Kirschner, K. N.; Woods, R. J. Solvent interactions determine carbohydrate conformation. *Proc. Natl. Acad. Sci. U.S.A.* **2001**, *98*, 10541–10545.
- (39) Kirschner, K. N.; Woods, R. J. Quantum mechanical study of the nonbonded forces in water-methanol complexes. *J. Phys. Chem. A* **2001**, *105*, 4150–4155.
- (40) Dapprich, S.; Komaromi, I.; Byun, K. S.; Morokuma, K.; Frisch, M. J. A new ONIOM implementation in Gaussian98. Part I. The calculation of energies, gradients, vibrational frequencies and electric field derivatives. *J. Mol. Struct.: THEOCHEM* **1999**, *461*, 1–21.
- (41) Maseras, F.; Morokuma, K. Imommm - a New Integrated Ab-Initio Plus Molecular Mechanics Geometry Optimization Scheme of Equilibrium Structures and Transition-States. *J. Comput. Chem.* **1995**, *16*, 1170–1179.
- (42) Cerqueira, N.; Fernandes, P.; Eriksson, L.; Ramos, M. Dehydration of ribonucleotides catalyzed by ribonucleotide reductase: The role of the enzyme. *Biophys. J.* **2006**, *90*, 2109–2119.
- (43) Cioslowski, J. A New Population Analysis Based on Atomic Polar Tensors. *J. Am. Chem. Soc.* **1989**, *111*, 8333–8336.
- (44) Fernandes, P. A.; Ramos, M. J. Theoretical studies on the mechanism of inhibition of ribonucleotide reductase by (E)-2'-fluoromethylene-2'-deoxycytidine-5'-diphosphate. *J. Am. Chem. Soc.* **2003**, *125*, 6311–6322.
- (45) Sousa, S. F.; Fernandes, P. A.; Ramos, M. J. General performance of density functionals. *J. Phys. Chem. A* **2007**, *111*, 10439–10452.
- (46) Cerqueira, N.; Fernandes, P. A.; Ramos, M. J. Enzyme ribonucleotide reductase: Unraveling an enigmatic paradigm of enzyme inhibition by furanone derivatives. *J. Phys. Chem. B* **2006**, *110*, 21272–21281.
- (47) Fernandes, P. A.; Eriksson, L. A.; Ramos, M. J. The reduction of ribonucleotides catalyzed by the enzyme ribonucleotide reductase. *Theor. Chem. Acc.* **2002**, *108*, 352–364.

CT1002175